JGR Space Physics

RESEARCH ARTICLE
10.1029/2019JA027619

Interaction of Cold Streaming Protons with the Reconnection Process

P. Tenfjord[1], M. Hesse[1,2], C. Norgren[1], S. F. Spinnangr[1], H. Kolstø[1], and N. Kwagala[1]

[1]Space Plasma Physics Group, University of Bergen, Bergen, Norway, [2]Southwest Research Institute, San Antonio, TX, USA

Key Points:
- Cold streaming protons flowing aligned with the upstream magnetic field cause the *X* line to move at the total mass velocity
- The reconnection rate is unaffected by the streaming velocity
- On the tailward side E_z remains laminar, whereas the E_z structure broadens and protons become more thermalized at the Earthward side

Supporting Information:
- Supporting Information S1

Correspondence to:
P. Tenfjord,
paul.tenfjord@ift.uib.no

Citation:
Tenfjord, P., Hesse, M., Norgren, C., Spinnangr, S. F., Kolstø, H., & Kwagala, N. (2020). Interaction of cold streaming protons with the reconnection process. *Journal of Geophysical Research: Space Physics*, *125*, e2019JA027619. https://doi.org/10.1029/2019JA027619

Received 8 NOV 2019
Accepted 18 MAR 2020
Accepted article online 29 APR 2020

Abstract We employ a 2.5D particle-in-cell simulation to study a scenario where the reconnection process captures cold streaming protons. As soon as the tailward streaming protons become involved, they contribute to the overall momentum balance, altering the initially symmetric dynamics. Adding tailward-directed momentum to the reconnection process results in a tailward propagation of the reconnection site. We investigate how the reconnection process reorganizes itself due to the changing momentum conditions on the kinetic scale and how the reconnection rate is affected. We find that adding tailward momentum does not result in a significantly different reconnection rate compared to the case without cold streaming protons, when scaled to the total Alfvén velocity. This implies that the effect of changing inflow conditions due to the motion of the reconnection site appears to be minimal. The dynamics of the particles are, however, significantly different depending on whether they enter on the tailward or Earthward side of the reconnection site. On the Earthward side they are reflected and thermalized, while on the tailward side they are picked up and accelerated. The cold proton density and E_z on the Earthward side are turbulent, while the tailward side has laminar cold proton density striations and an embedded E_z layer. Also, since the initial plasma sheet population is swept up on one side and flushed out on the other, asymmetries in the densities and strength of Hall fields emerge. Our results are important for understanding the development and dynamics of magnetospheric substorms and storms.

1. Introduction

Magnetic reconnection describes the process facilitating the release of stored electromagnetic energy into mechanical (kinetic and thermal) energy of the plasma, producing a global change of the magnetic configuration due to local decoupling of plasma from the magnetic field. In many plasma systems this intricate interaction between the fields and particles includes populations with different properties, such as heavy ions, cold ions, streaming populations, or a combination of these (Kistler & Mouikis, 2016). The presence of additional ion populations can, if magnetized, mass load the system, and the resulting reduction of the Alfvén velocity is believed to be a mechanism, which can slow down reconnection (Hesse & Birn, 2004; Shay & Swisdak, 2004). In addition to the mass-loading effect, other mechanisms such as the effect of heavy ions on the tearing growth rate (Karimabadi et al., 2011) and induced ambipolar (charge separation) electric fields (Liang et al., 2016, 2017) have been suggested. Heavy ions, such as O^+ (and their accompanying electrons), have been found to affect the reconnection process by extracting energy from the system that would otherwise go to the protons, thereby significantly reducing the reconnection rate, but less than expected by mass loading (Kolstø et al., 2020; Tenfjord et al., 2018, 2019).

Magnetic reconnection in the presence of shear (oppositely directed) flow has previously been investigated in detail (Cassak, 2011; Cassak & Otto, 2011; Mitchell & Kan, 1978). Reconnection occurs for such configurations in, for instance, tokamaks, at the dayside magnetopause (especially during northward directed interplanetary magnetic field) (e.g., Gosling et al., 1986; La Belle-Hamer et al., 1995) and in the magnetosheath (Eriksson et al., 2018). Based on theoretical arguments and fluid simulations, it is believed that such flow will reduce the reconnection rate by effectively reducing part of the magnetic tension that drives the outflow (Cassak, 2011). It has also been observed that shear flow causes the outflow jet and current sheet to tilt (La Belle-Hamer et al., 1994) and causes a configuration that is susceptible to tearing mode and Kelvin-Helmholtz instabilities (Chen et al., 1997; Li & Ma, 2010; Roytershteyn & Daughton, 2008).

Varying conditions in the inflow regions, such as different plasma populations or plasma properties, can also have an impact on the reconnection process. On the dayside, the effect of plasmaspheric drainage plumes has been found to mass load the reconnection site, thereby reducing the effective solar wind magnetosphere coupling (Borovsky & Denton, 2006; Dargent et al., 2020). However, the effect of ions originating from the ring current and warm plasma cloak has been observed not to greatly affect the reconnection rate (Fuselier et al., 2016; Wang et al., 2015). Another source of heavy ions on the dayside is O^+ originating from the high-latitude ionosphere. During northward directed IMF B_z dual-lobe reconnection can trap O^+ and mass load the dayside magnetopause boundary, which may affect the reconnection rate (Fuselier et al., 2019). On both the dayside and nightside, observations show that the involvement of additional cold, dense plasma or plasma beams can alter the dynamics of the reconnection process, affect the reconnection rate, and modify the Hall term in Ohms law (Li et al., 2017; Toledo-Redondo et al., 2018; Xu et al., 2019). Since the Larmor radius depends on the mass and velocity, these different ion populations will lead to a different kinetic behavior and additional scale lengths in the system (Alm et al., 2019; André et al., 2016; Dargent et al., 2019; Divin et al., 2016; Toledo-Redondo et al., 2015).

In this manuscript we study how a streaming population is captured by the reconnection process and what the effects are. This scenario is studied using a 2.5D particle-in-cell (PIC) simulation where a cold streaming population is inserted in the two lobes and eventually is captured by the reconnection process. Scenarios where streaming populations interact with magnetic reconnection can be attributed to ionospheric ion outflow (characteristically observed as cold ions with a parallel velocity), streaming mantle interaction, or high-latitude magnetopause reconnection where streaming magnetosheath interacts with the magnetopause. Ion outflow from the high-latitude ionosphere is believed to be a significant source of plasma for the terrestrial magnetosphere (Chappell et al., 1980; Haaland, Svenes, et al., 2012). These ions (mostly O^+ and H^+) flow parallel to the magnetic field and fill the lobes with streaming low-energy ions. The outward velocity is typically observed to be up to ≈50 km/s (André et al., 2015; Haaland, Li, et al., 2012). The Earth's plasma mantle is one of the major suppliers of particles for the plasma sheet. The plasma mantle was first reported by Rosenbauer et al. (1975), as a persistent layer of tailward-flowing magnetosheath-like plasma inside of and adjacent to the magnetopause. The tailward-directed parallel flow speed was found to usually lie between 100–200 km/s and always less than the adjacent magnetosheath flow velocity. Observations from ARTEMIS reported an average temperature of about ≈0.05–0.2 keV and density ≈0.1–1 cm^{-3} (Wang et al., 2014). Magnetotail observations have revealed that the distant plasma mantle can occur even near the equatorial plane (Schillings et al., 2019; Siscoe et al., 1994; Taguchi et al., 2001). In our simulation we have chosen the streaming velocity of $v = 0.5V_A$, which should be considered as an extreme (based on a lobe magnetic field of $B_0 = 20$ nT and a current sheet density of $n_0 = 0.2$ cm^{-3}, the Alfvén velocity is 1,000 km/s, which would correspond to a streaming velocity of 500 km/s).

The manuscript is organized as follows: In Section 2 we describe the simulation setup. Section 3 describes the motion of the X line as the streaming cold plasma interacts with the reconnection process. In Section 4 we show specific velocity distributions, representative ion particle trajectories, and describe which forces these particles experience during their evolution. In Section 5 we discuss the asymmetries in the Hall electric field and the additional scale length introduced by the cold plasma population. In Section 6 we compare the reconnection rate of our simulation to a separate simulation without cold streaming ions and discuss how the streaming plasma population affects the rate. A discussion and a summary are given in Section 7.

2. Simulation Setup

The simulation is designed to study how a streaming population is captured by the reconnection process. The streaming protons and electrons are chosen to have zero temperature and a streaming velocity of $v_x = 0.5V_A$ on both sides of the neutral sheet. We employ a 2.5D (two spatial dimensions [x and z] and three velocity dimensions [x, y, and z]) PIC, which has previously been applied to a variety of reconnection problems (e.g., Hesse et al., 2001, 2018; Tenfjord et al., 2018, 2019). The initial magnetic field configuration is a two-dimensional generalized Harris-type equilibrium (see Hesse & Bern, 2004, for details) with zero guide field ($B_y = 0$). It is defined as $B_x = B_0 \tanh(z/\lambda)$, where $\lambda = 2d_p$ is the half-width of the current sheet layer. Lengths are normalized to the proton inertial length: $d_p = c/\omega_{pi}$. Time is normalized to the inverse of the proton cyclotron frequency: Ω_p^{-1}. All calculations use a proton/electron mass ratio of $m_p/m_e = 25$. A total of $\sim 1 \cdot 10^{10}$ macroparticles are employed, divided equally between the four species (warm protons, warm electrons, streaming cold protons, and streaming cold electrons). Boundary conditions are periodic at

$x = 0$ and $x = x_{max}$. At the upper and lower boundaries, we employ specular reflection for particles, and the out-of-plane electric field is set to 0, implying flux conservation in the simulation domain. Our simulation domain size is $400 \times 50 d_p$, divided into a grid of $6,400 \times 1,600$ cells. The grid is extended in the x-direction to account for the X-line propagation. A time step of $\omega_{pe}\delta t = 0.5$ is employed. The density is normalized to the foreground current sheet density n_0 (unity), which supports the initial Harris sheet equilibrium. The velocity is normalized to the proton Alfvén speed, based on n_0, and the electric field is normalized by $V_A B_0$. The foreground temperatures fulfill $T_p + T_e = 0.5 m_p V_A^2$, and proton-to-electron temperature ratio is $T_p/T_e = 5$. The ratio between the electron plasma frequency and gyrofrequency is $\omega_{pe}/\Omega_{ce} = 2$. The presented data are displayed in normalized units. A uniformly distributed proton (H^+) background with $n_p = 0.2$ is added to the Harris sheet density distribution, which leads to a peak density of $n = 1.2$. In addition to the uniform H^+ population, the cold streaming population with number density $n_c = 0.8$ is added to the inflow regions ("lobes"), above and below a specific field line, approximately at $|z| > 3d_i$ where the initial magnetic field perturbation is centered. We use the term "cold protons" (and the accompanying cold electrons) for the initially cold species inserted in the beginning of the simulation, even though they thermalize throughout the simulation and get heated. The cold protons do not contribute to the total pressure, so the plasma $\beta = 0.2$ remains unchanged at 0.2 in the inflow. In our simulation we reserved the first 40 time steps for the system to equilibrate. During this period the cold electrons are somewhat heated numerically. For comparisons we also use output from a previous simulation used in Tenfjord et al. (2018).

3. Motion of *X* line

Reconnection initiates with warm nonstreaming populations only, and the reconnection site does not move. When the momentum-laden streaming cold ions are captured by the reconnection process, the momentum balance of the system is altered, causing a motion of the reconnection site in the direction of the streaming plasma. Figure 1 shows the cold streaming proton density, warm proton density, and the Hall electric field E_z at four different times (a video of the evolution is provided as supporting information). In Figure 1, $t = 0$ represents the initial configuration, showing how the cold protons are distributed at the beginning of the simulation. At $t = 72$ the cold protons become involved in the reconnection process, and in the following time steps a tailward (toward the right) motion of the X line is apparent. This shows that once a sufficient amount of tailward-directed plasma has been captured by the reconnection process, the system reorganizes itself to incorporate the additional x-directed momentum by facilitating a tailward-directed motion of the X line. The Earthward (toward left) outflow region is stretched by the motion of the X line. On the opposite side, the outflow region is compressed, and the Hall field is broader in the z-direction. The x-directed velocity of the X line is determined by the total mass velocity:

$$v_{mass} = \frac{\sum m_s n_s v_s}{\sum m_s n_s} = 0.35, \tag{1}$$

where the sum is taken over all plasma populations (warm protons, streaming protons, and the electrons) over the entire simulation domain. As seen in Figure 1, the streaming population gets involved around $t = 72$. After a short transition period ($\sim 5\ \Omega_p^{-1}$) the X line moves at a constant velocity determined by the total mass velocity. Such a convection velocity is expected based on fluid arguments; see Doss et al. (2015) for expected convection velocities and densities in the case of asymmetric magnetic reconnection.

In Figure 2 we show the in-plane velocity vectors and the x-directed velocity as background color. The top row shows the velocities in the simulation frame for the warm protons, cold streaming protons, and the total mass flow. The bottom row shows the same quantities transformed into the frame moving with the reconnection site (equal to total mass velocity). From these panels it is apparent that the reconnection process has facilitated the tailward propagation of the reconnection site so that in its frame of reference the inflow and outflow remain symmetric. In the next section we look in greater detail at the dynamics of the particles and how they lead to the tailward motion of the X line.

4. Particle Interactions

In Figure 3 we show velocity distributions of the cold protons taken at $z = 0$ and seven different x locations. At this time, $t = 100$, the X line is located at approximately $x \sim 215$. On the right side of the X line the distributions consist of two cold counterstreaming populations. At this location and further tailward, the

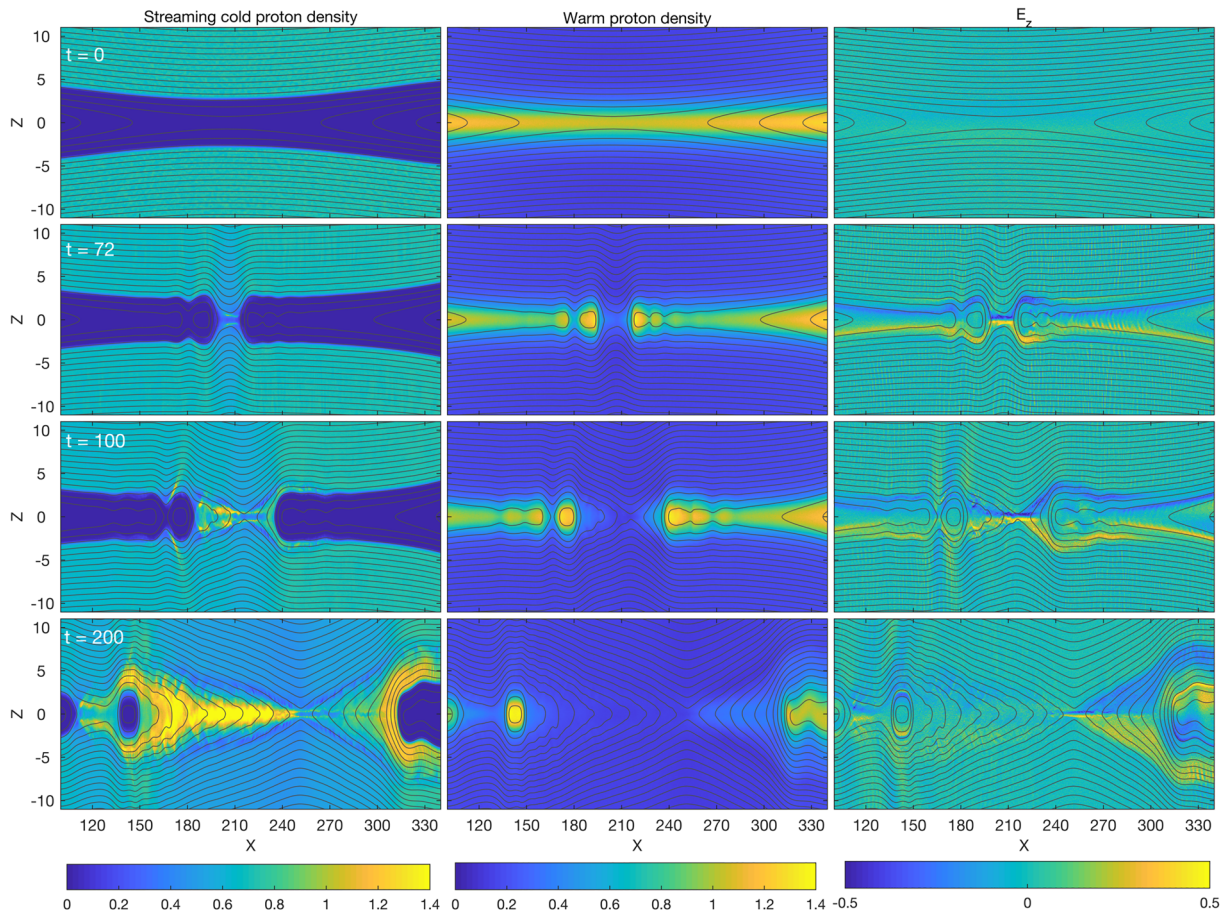

Figure 1. Cold streaming proton density, warm proton density, and E_z electric shown for four different times. The cold population is streaming in the positive x-direction with a velocity of $v = 0.5V_A$. See text for details.

cold population undergoes meandering motions as they are streaming tailward. Thus, if a particle enters the exhaust to the right of the X line, it gets picked up and accelerated in the positive x-direction, while performing meandering motions. This behavior is seen in Figure 4 for the rightmost particle, where the particle enters the diffusion region from the southern lobe and is ejected to the tailward exhaust. This motion results in cold proton density striations (see Figure 4), visible above and below the current sheet. The striations extend in the tailward direction with a velocity that corresponds to the flux velocity (frozen in). Downstream, the density striations become progressively weaker and eventually disappear due to particle scattering in the curved magnetic field.

These clear density striations in the tailward exhaust are a signature that the cold streaming protons are confined and that the vertical distance corresponds to their meandering width (which in turn is related to their thermal energy). This layer and the asymmetries between the two exhaust regions will be discussed in Section 5.

On the Earthward (left) side of the X line the velocity distributions are different. Figure 3 for $x = 195$ shows cold protons with both positive and negative v_x. By following a test particle from this region, we see that the particles that have a negative v_x represent incoming particles that have been reflected (Figure 4), while the population with positive x-velocity is inbound, not yet reflected. Compared to the tailward side, the distribution here becomes largely thermalized, which produces a more turbulent region with fluctuations in both density and E_z (discussed in Section 5).

To understand which forces cause a particle to reverse its x-velocity we show, in Figure 5, the forces acting on the particle, which passes through $x = 213$ at $t = 100$. At $t = 100$ (indicated by the black vertical line), the particle has the velocity: $(v_x, v_y, v_z) = (0.3, -0.1, 0.5)$. From this time the particle is traced forward and backward in time based on interpolations of the dynamically changing fields, which are updated every 0.2

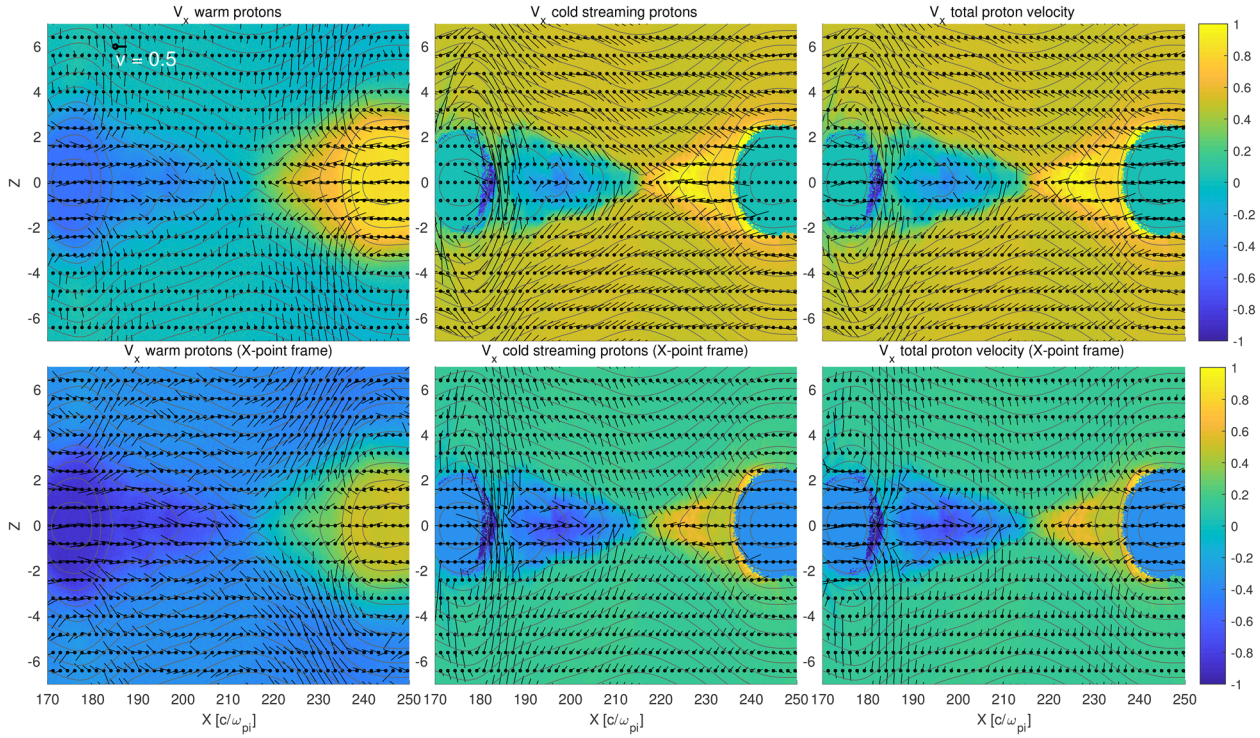

Figure 2. In-plane velocities of the warm, cold, and combined ion populations in the simulation frame (top row) and the frame moving with the X line at $t = 100$. The quivers show the in-plane velocity as wind vectors (the amplitude $v = 0.5$ is indicated in the top left panel), while the color map shows v_x. In the frame moving with the reconnection site, the total mass velocity of the inflow and outflow remains symmetric.

Ω_p^{-1}. Once the particle enters the diffusion region ($t > 100$), it gets a significant y-directed velocity by the reconnection electric field. Meanwhile, in the x-direction, a combination of E_x and, to a lesser degree, $v_y B_z$ reverses v_x from positive to negative (seen in Figure 5 at $t > 100$).

Ions that reverse their x-directed velocity all experience a significant E_x field, as for the particle analyzed in Figure 5. Figure 6 shows the smoothed magnitude of E_x and $\int E_x dx$ along x for $z = 0$. At this time, the X line is at $x = 219$. A significant negative E_x exists in the range $x = 195 - 215$, which coincides with the location where the cold protons are turned around, at this time. To the right of the X-line location, at $x = 225-240$, a positive but weaker E_x exists. The asymmetry of E_x between the tailward and Earthward side is a consequence of the streaming motion of the cold plasma. In contrast to the ions, the electrons that enter the exhaust left of the X line will get magnetized and will be "picked up" by flux tubes moving Earthward. A relatively strong E_x will then be induced in order to turn around the tailward streaming protons and to

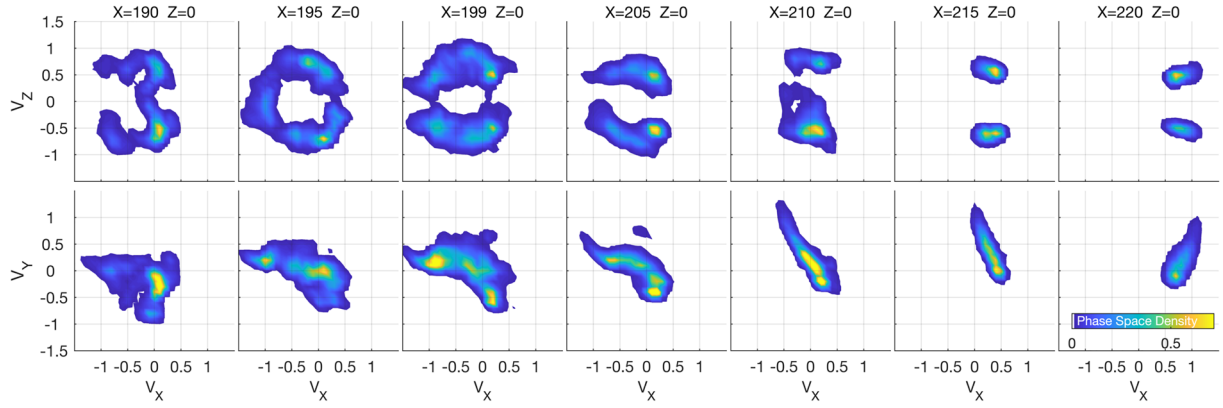

Figure 3. Velocity distributions of the cold streaming population taken at different x-location along $z = 0$ at $t = 100$. A bin size of $(dx, dz) = (0.5,0.5)$ is used to accumulate the distribution.

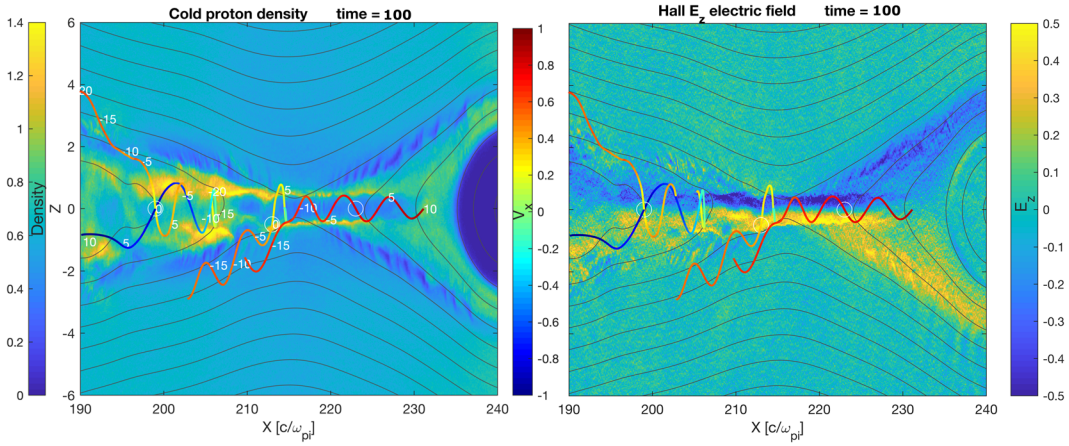

Figure 4. Cold proton density (left) and E_z electric field (right) with particle trajectories overlaid. The trajectories are color coded corresponding to their x-directed velocity. The particles are traced 20 Ω_p^{-1} backward and 10 Ω_p^{-1} forward from the white circles. A video of how the fields evolve during the particles evolution can be found in the supporting information.

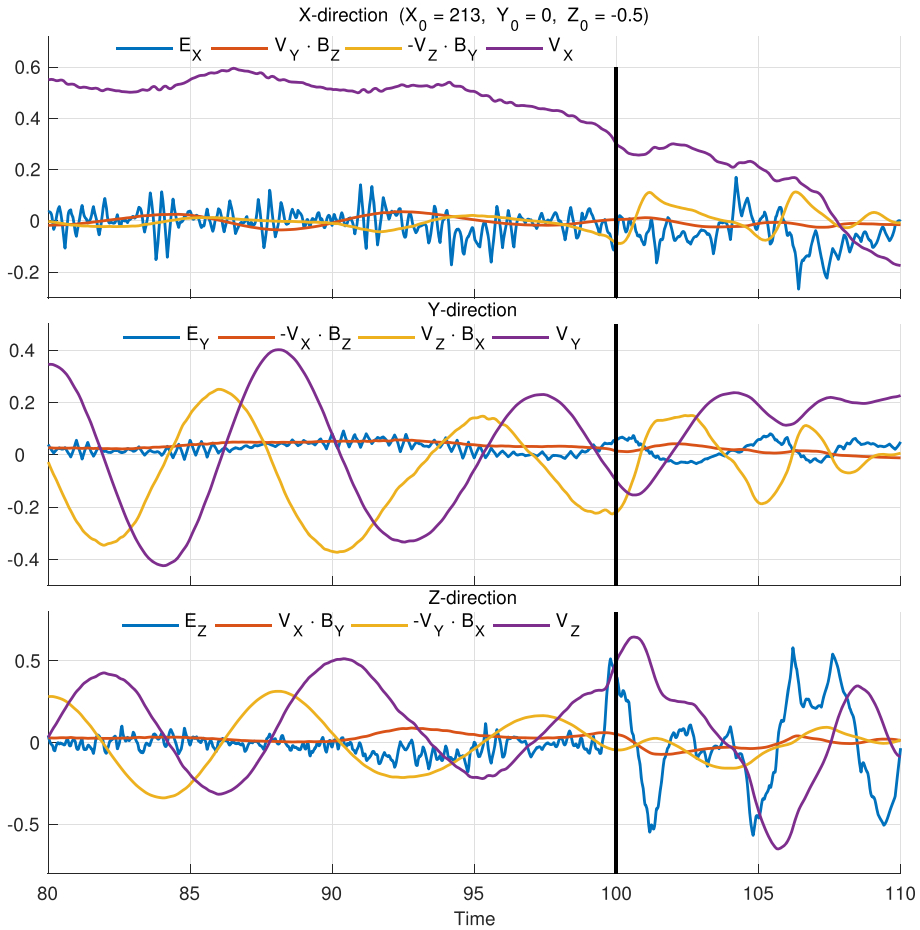

Figure 5. Forces acting on particle that passes through $x = 213$ and $z = -0.5$ at $t = 100$ (marked by the vertical line). The particle starts in the southern lobe with an x-directed velocity of approximately 0.5; after performing a couple of bounces its positive x-directed motion is turned into a negative v_x, primarily by a negative E_x. In the time it spent inside the diffusion region it also gained a positive y-directed motion, and the force from $v_y B_z$ also has a net contribution in the negative direction in the later stage of the evolution.

Figure 6. Cut through $z = 0$ at $t = 110$, showing asymmetry in E_x between the right and left outflow locations. The E_x on the left side is necessarily stronger so that the tailward momentum of the streaming cold protons can be turned into Earthward motion. Contrary to the tailward side where the cold protons enter with a tailward momentum, which only gets further increased by E_x.

accelerate the cold protons that have been turned around so that quasineutrality is maintained. The particles that enter to the right of the X line are to a much lesser degree affected by the above effect, since they already carry a tailward direction motion. Only a relatively small E_x is therefore needed to sustain the outflow.

5. Asymmetries in E_z

As seen in Figure 1 (also seen in Figure 4), the tailward side has a smaller E_z region embedded in the larger Hall structure, whose width is comparable to the Earthward-side Hall field. This embedded E_z region is not unique to this simulation and was produced on both sides prior to the involvement of the cold streaming protons. These electron-scale structures have been seen in numerous simulations (Chen et al., 2011; Liang et al., 2017; Shay et al., 1998; Zhou et al., 2012) and are attributed to electron meandering motions (Drake et al., 2008; Shuster et al., 2015). However, when the cold streaming protons get involved, an asymmetry between the two sides of the exhaust emerges. The density and E_z electric field on the Earthward side are turbulent, while the tailward side has laminar cold proton density striations and an embedded E_z layer.

The larger Hall region on the tailward side, extending up toward and along the separatrices, is generated by the warm protons and is a result of the tailward motion of the X line sweeping up warm plasma sheet protons that were originally part of the initial plasma sheet population. This is in contrast to the Earthward side where the warm plasma sheet population is flushed out and replaced with the cold proton population. This can be seen in Figure 1. On the Earthward side the cold protons now dominate the number density.

In Figure 4 we see the rightmost, tailward-directed particle entering the diffusion region from the southern lobe with a streaming velocity of $v_x = 0.5V_A$. In Figure 3 at $X = 215$ and $x = 220$, we see that the cold protons found within the embedded E_z layer form two cold counterstreaming beams. The density striations seen in Figure 4 are therefore a result of the cold protons being confined and bouncing in this preexisting E_z layer. The thermal energy of the cold protons confined in this embedded layer ($-0.5 \lesssim z \lesssim 0.5$) is comparable to the convection corrected potential ($\Phi \sim \int E_z' dz = \int (E_z + v_x B_y - v_y B_x) dz$) they experience in the frame moving with the average velocities.

Since the thermal energy of the cold protons confined in this layer is comparable to the convection corrected potential, it appears that the inner E_z layer is shaped by a combination of electron and cold ion bounce motion (after being established by electrons alone).

On the Earthward side this influence is prominent. The electron-scale E_z layer, which existed prior to the cold protons involvement, has disappeared and been replaced by a much broader, turbulent structure. Figure 3 shows that the cold proton population to the left of the X line ($X < 215$) is more thermalized. Their thermal energy is too high to confine them in the same way as on the tailward side, and the laminar embedded E_z

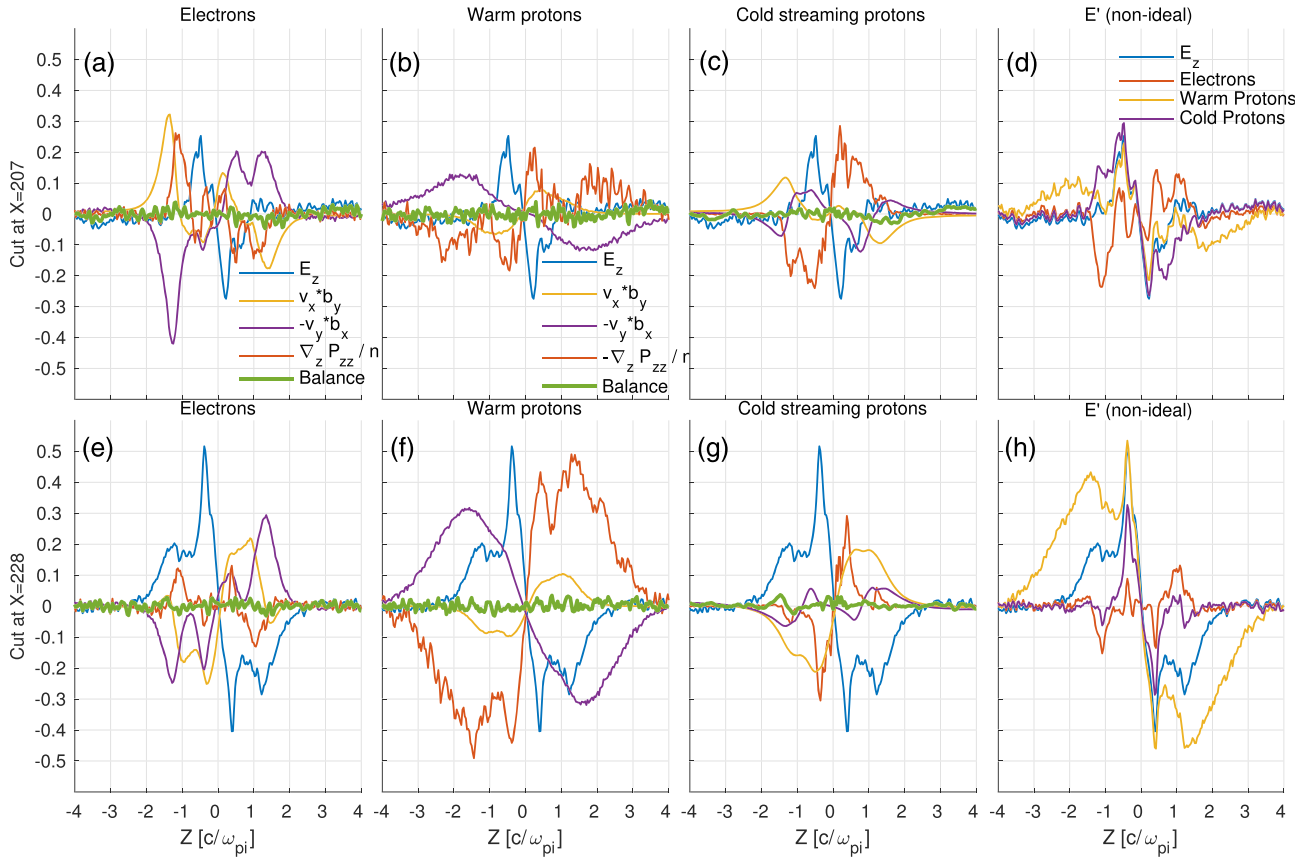

Figure 7. Momentum balance for each species at two z cuts at $t = 110$. The inertia terms (calculated with time step 0.2 Ω_p^{-1}) are small and not shown but included in the sum. The figure shows significant asymmetries in the strength and width of the Hall E_z electric field between the Earthward (top row) and tailward (bottom row) side. On the Earthward side (panels a–d) the warm plasma population has been flushed out and replaced by lobe densities (mostly cold streaming protons), resulting in a narrow and weaker Hall field. On the tailward side (panels e–h) the warm plasma sheet has been swept up by the motion of the X line, resulting in a thicker Hall region, with a smaller region embedded inside, whose width corresponds to the cold proton meandering width.

layer that existed earlier has broken up and evolved into a turbulent region. This occurs in combination with the warm population having been flushed out by the motion of the X line, and the new "Hall" layer is primarily due to thermalized cold protons.

In Figure 7 we show the momentum balance for the warm and cold streaming protons ($E_z + v_x^i B_y - v_y^i B_x - \frac{\partial}{n^i \partial z} P^i_{zz} - inertia = 0$) and the combined electron population ($E_z + v_x^e B_y - v_y^e B_x + \frac{\partial}{n^e \partial z} P^e_{zz} + inertia = 0$) at $x = 207$ and $x = 228$. These two locations are about $10d_i$ to each side from the active X line at $t = 110$. For the cold protons at the Earthward side (Figure 7c), the Hall electric field is balanced mainly by the thermal pressure. This shows that the cold protons get thermalized by the complicated motion, which includes reversing the x-directed motion (Figures 4 and 5). Since the majority of the warm plasma sheet protons, which initially preserved force balance, have been pushed out and replaced by cold protons, the vertical spatial extent of the Hall electric field has therefore decreased to a characteristic length dominated by the cold protons meandering width.

On the tailward side (Figure 7g), the cold streaming protons have not thermalized much, as seen in Figure 3 for $X = 220$. They continue with their tailward motion performing meandering motions as they are picked up by the outflow. At the same time, the warm plasma sheet protons are being swept up by the motion of the X line in the tailward direction. Therefore, contrary to the Earthward side, here the spatial extent of the Hall E_z is still dominated by the warm protons' characteristic scale length (Figure 7f), with the embedded E_z layer corresponding to the confined and bouncing cold protons. Figure 7g shows that for the cold protons E_z is balanced by $v \times B$ forces in the broader diffusion region, while the thermal pressure becomes significant at $|z| < 0.5$, corresponding to the strong peak in E_z seen at these locations. In Figure 7f, E_z is balanced by

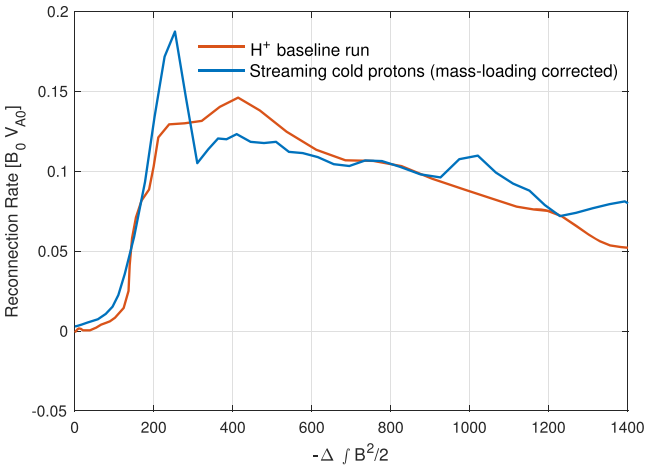

Figure 8. Comparing the mass-loading-corrected reconnection rate to a baseline run without cold protons. The blue line shows the reconnection rate the simulation with streaming cold, scaled by $\sqrt{(n_p+n_c)/(n_p)}=2.23$ (mass loading corrected). After correcting for the additional mass, there is no significant effect of the streaming cold proton population on the reconnection rate.

the warm protons thermal pressure, which has a significantly larger scale length on the tailward side ($\sim 3d_i$) compared to the Earthward side ($\leq 1d_i$).

Figures 7d and 7h also show the location where each species is no longer frozen in, denoted by the violation of the condition $E'=E+v\times B=0$. As expected, the warm population violates the frozen-in condition over a larger region, while the electrons and the cold protons both violate the frozen-in condition over smaller regions. The fact that the cold protons and electrons appear to have comparable scale lengths is related to the cold protons being confined in the electron-scale embedded E_z. Additionally, it could also be influenced by our mass ratio and may be related to the heating of electrons during the period when the system equilibrates (see Section 2).

6. Reconnection Rate

In Figure 8 we show the mass-corrected reconnection rate and compare it to the reconnection rate of a simulation without cold plasma but otherwise identical. The reconnection rate is first calculated as $\frac{d}{dt}\Phi_{rec}=\int E_y dy$ and thereafter scaled to $v_A(n=n_c+n_p)/v_A(n=n_c)=\sqrt{(n_c+n_p)/n_p}=2.23$ (ratio between Alfvén velocities with and without including cold ions). The x-axis is the change of magnetic energy from the initial magnetic state. Presenting the reconnection rate as a function of spent magnetic energy allows us to compare the rates when the two different simulations are at the same evolutionary stage. The blue line is the reconnection rate for the simulation discussed in this manuscript. If we compare the rate of the streaming cold protons run to the baseline run there is a slight offset, but in general, the difference in the reconnection rate is well explained by simple mass loading. This is in agreement with previous numerical simulation of cold ions, which are not streaming (Dargent et al., 2017, 2020; Divin et al., 2016). This study shows that there does not appear to be any additional effect of streaming proton-reconnection interaction on the reconnection rate.

Thus, even though the motion of the X line causes the reconnection site to propagate downstream, into a region of unperturbed inflow conditions, it appears that this does not lead to an additional decrease in the reconnection rate.

7. Discussion and Summary

In this study we have found that the addition of a tailward propagating cold species causes the reconnection site to move tailward with a velocity corresponding to the total mass velocity. This means that once a sufficient amount of tailward-directed plasma has been captured by the reconnection process, the system reorganizes itself to incorporate the additional x-directed momentum by facilitating a tailward-directed motion of the X line. In the frame of the moving X line, both the inflow and outflow are then organized symmetrically.

As the propagating cold species is captured by the reconnection process, they are either turned around if they enter some distance to the left of the X line or further accelerated if they enter some distance to the right of the X line. The velocity distributions (Figure 3) show that particles coming into the outflow region with a positive v_x are mixed with particles that have previously entered and turned around. This results in circular v_x-v_z distributions (Figure 3).

The tailward motion causes asymmetries in the reconnection geometry, elongating the current sheet on one side and broadening it on the opposite side. Large asymmetries between the two outflow directions arise due to the presence of cold streaming proton population. The tailward propagation of the X line sweeps up the warm plasma on the tailward side, while it is flushed out on the opposite side. This results in a thicker Hall region on the side where warm protons are present. In addition to this extended Hall layer, an embedded E_z layer with a significant smaller vertical extent is present. Cold protons are confined and meandering inside this structure, producing laminar density striations. On the Earthward side, the streaming cold protons are thermalized by the complicated motion, which includes reversing the x-directed motion. This leads to a smeared out, more turbulent region with fluctuations in both density and E_z. An additional asymmetry in E_x between the two outflow regions arises as a result of the tailward streaming cold protons getting reflected

in the x-direction on the Earthward side, causing a larger charge imbalance compared to the tailward side, where they experience an acceleration in the same direction they were initially streaming in. By comparing our simulation to a simulation that did not include cold streaming protons, we found that the inclusion of an additional cold species reduces the reconnection rate as predicted by mass loading, regardless of the species tailward propagation. Although we simulate a cold streaming population, we expect that similar effects would occur for a warm streaming population. We would however expect the kinetic substructures to be more smeared out.

Our results are important for understanding the development and dynamics of magnetospheric substorms and storms. We have shown that streaming plasma can effectively move the reconnection site. In both the magnetotail and on the dayside streaming protons can move the reconnection site into regions where the magnetic field is weaker, which would result in effective reduction or even cessation of reconnection. In addition, especially for the magnetotail, the Earthward outflow velocity is reduced (by a factor corresponding the mass velocity) leading to a potential reduction of the ionospheric response.

Acknowledgments
The authors acknowledge helpful and constructive comments by Jason Shuster and Jérémy Dargent who made very helpful suggestions, especially regarding the embedded E_z layer discussed in Section 5. Their suggestions improved our interpretation. This study was supported by the Research Council of Norway/CoE under Contract 223252/F50, by NOTUR/NORSTOR under Project NN9496K, and by NASA's MMS mission. We also acknowledge the support of the ISSI's international team on "Cold plasma of ionospheric origin at the Earth's magnetosphere" and all its members: Sergio Toledo-Redondo, Mats Andre, Nicolas Aunai, Charles R. Chappell, Stephen Fuselier, Alex Glocer, Stein Haaland, Lynn Kistler, Benoit Lavraud, Wenya Li, Thomas E. Moore, Daniel B. Graham, Love Alm, Jeremy Dargent, and Sarah Vines. Data set used in this analysis is available at https://doi.org/10.18710/MEYFPM (Tenfjord, 2020).

References

Alm, L., André, M., Graham, D. B., Khotyaintsev, Y. V., Vaivads, A., Chappell, C. R., et al. (2019). MMS observations of multiscale Hall physics in the magnetotail. *Geophysical Research Letters*, *46*, 10,230–10,239. https://doi.org/10.1029/2019GL084137

André, M., Li, K., & Eriksson, A. I. (2015). Outflow of low-energy ions and the solar cycle. *Journal of Geophysical Research: Space Physics*, *120*, 1072–1085. https://doi.org/10.1002/2014JA020714

André, M., Li, W., Toledo-Redondo, S., Khotyaintsev, Y. V., Vaivads, A., Graham, D. B., et al. (2016). Magnetic reconnection and modification of the Hall physics due to cold ions at the magnetopause. *Geophysical Research Letters*, *43*, 6705–6712. https://doi.org/10.1002/2016GL069665

Borovsky, J. E., & Denton, M. H. (2006). Effect of plasmaspheric drainage plumes on solar-wind/magnetosphere coupling. *Geophysical Research Letters*, *33*, 2–6. https://doi.org/10.1029/2006GL026519

Cassak, P. A. (2011). Theory and simulations of the scaling of magnetic reconnection with symmetric shear flow. *Physics of Plasmas*, *18*(7), 072106. https://doi.org/10.1063/1.3602859

Cassak, P. A., & Otto, A. (2011). Scaling of the magnetic reconnection rate with symmetric shear flow. *Physics of Plasmas*, *18*(7), 1–4. https://doi.org/10.1063/1.3609771

Chappell, C. R., Baugher, C. R., & Horwitz, J. L. (1980). New advances in thermal plasma research. *Reviews of Geophysics*, *18*(4), 853–861. https://doi.org/10.1029/RG018i004p00853

Chen, L. J., Daughton, W. S., Lefebvre, B., & Torbert, R. B. (2011). The inversion layer of electric fields and electron phase-space-hole structure during two-dimensional collisionless magnetic reconnection. *Physics of Plasmas*, *18*(1), 1–8. https://doi.org/10.1063/1.3529365

Chen, Q., Otto, A., & Lee, L. C. (1997). Tearing instability, Kelvin-Helmholtz and magnetic reconnection. *Journal of Geophysical Research*, *102*, 151–161.

Dargent, J., Aunai, N., Lavraud, B., & Califano, F. (2020). Simulation of plasmaspheric plume impact on dayside magnetic reconnection. *Geophysical Research Letters*, *47*(4), e2019GL086546. https://doi.org/10.1029/2019GL086546

Dargent, J., Aunai, N., Lavraud, B., Toledo-Redondo, S., & Califano, F. (2019). Signatures of cold ions in a kinetic simulation of the reconnecting magnetopause. *Journal of Geophysical Research: Space Physics*, *124*, 2497–2514. https://doi.org/10.1029/2018JA026343

Dargent, J., Aunai, N., Lavraud, B., Toledo-Redondo, S., Shay, M. A., Cassak, P. A., & Malakit, K.(2017). Kinetic simulation of asymmetric magnetic reconnection with cold ions. *Journal of Geophysical Research: Space Physics*, *122*, 5290–5306. https://doi.org/10.1002/2016JA023831

Divin, A., Khotyaintsev, Y. V., Vaivads, A., André, M., Toledo-Redondo, S., Markidis, S., & Lapenta, G. (2016). Three-scale structure of diffusion region in the presence of cold ions. *Journal of Geophysical Research: Space Physics*, *121*, 12,001–12,013. https://doi.org/10.1002/2016JA023606

Doss, C. E., Komar, C. M., Cassak, P. A., Wilder, F. D., Eriksson, S., & Drake, J. F. (2015). Asymmetric magnetic reconnection with a flow shear and applications to the magnetopause. *Journal of Geophysical Research A: Space Physics*, *120*, 7748–7763. https://doi.org/10.1002/2015JA021489

Drake, J. F., Shay, M. A., & Swisdak, M. (2008). The Hall fields and fast magnetic reconnection. *Physics of Plasmas*, *15*(4), 1–10. https://doi.org/10.1063/1.2901194

Eriksson, E., Vaivads, A., Graham, D. B., Divin, A., Khotyaintsev, Y. V., Yordanova, E., et al. (2018). Electron energization at a reconnecting magnetosheath current sheet. *Geophysical Research Letters*, *45*, 8081–8090. https://doi.org/10.1029/2018GL078660

Fuselier, S., Burch, J. L., Cassak, P. A., Goldstein, J., Gomez, R. G., Goodrich, K., et al. (2016). Magnetospheric ion influence on magnetic reconnection at the duskside magnetopause. *Geophysical Research Letters*, *43*, 1435–1442. https://doi.org/10.1002/2015GL067358

Fuselier, S., Trattner, K., Petrinec, S., Denton, M., Toledo-Redondo, S., André, M., et al. (2019). Mass-loading the Earth's dayside magnetopause boundary layer and its effect on magnetic reconnection. *Geophysical Research Letters*, *3*, 6204–6213. https://doi.org/10.1029/2019gl082384

Gosling, J. T., Thomsen, M. F., Bame, S. J., & Russell, C. T. (1986). Accelerated plasma flows at the near-tail magnetopause. *Journal of Geophysical Research*, *91*(A3), 3029. https://doi.org/10.1029/ja091ia03p03029

Haaland, S. E., Li, K., Eriksson, A., André, M., Engwall, E., Förster, M., et al. (2012). Cold ion outflow as a source of plasma for the magnetosphere. *Geophysical Monograph Series*, *199*(May 1996), 341–353. https://doi.org/10.1029/2012GM001317

Haaland, S. E., Svenes, K., Lybekk, B., & Pedersen, A. (2012). A survey of the polar cap density based on Cluster EFW probe measurements: Solar wind and solar irradiation dependence. *Journal of Geophysical Research*, *117*, A01216. https://doi.org/10.1029/2011JA017250

Hesse, M., & Birn, J. (2004). On the cessation of magnetic reconnection. *Annales Geophysicae*, *22*, 603–612.

Hesse, M., Kuznetsova, M., & Birn, J. (2001). Particle-in-cell simulations of three-dimensional collisonless magnetic reconnecion. *Journal of Geophysical Research*, *106*(A12), 29–831. https://doi.org/10.1029/2001JA000075

Hesse, M., Liu, Y. H., Chen, L. J., Bessho, N., Wang, S., Burch, J. L., et al. (2018). The physical foundation of the reconnection electric field. *Physics of Plasmas*, *25*(3). https://doi.org/10.1063/1.5021461

Karimabadi, H., Roytershteyn, V., Mouikis, C. G., Kistler, L. M., & Daughton, W. (2011). Flushing effect in reconnection: Effects of minority species of oxygen ions. *Planetary Space Science*, *59*(7), 526–536. https://doi.org/10.1016/j.pss.2010.07.014

Kistler, L. M., & Mouikis, C. G. (2016). The inner magnetosphere ion composition and local time distribution over a solar cycle. *Journal of Geophysical Research: Space Physics*, *121*, 2009–2032. https://doi.org/10.1002/2015JA021883

Kolstø, H. M., Hesse, M., Norgren, C., Tenfjord, P., Spinnangr, S. F., & Kwagala, N. (2020). Collisionless magnetic reconnection in an asymmetric oxygen density configuration. *Geophysical Research Letters*, *47*, e2019gl085359. https://doi.org/10.1029/2019gl085359

La Belle-Hamer, A. L., Otto, A., & Lee, L. C. (1994). Magnetic reconnection in the presence of sheared plasma flow: Intermediate shock formation. *Physics of Plasmas*, *1*(3), 706–713. https://doi.org/10.1063/1.870816

La Belle-Hamer, A. L., Otto, A., & Lee, L. C. (1995). Magnetic reconnection in the presence of sheared flow and density asymmetry: Applications to the Earth's magnetopause. *Journal of Geophysical Research*, *100*(A7), 11,875–11,890. https://doi.org/10.1029/95ja00969

Li, W. Y., Andrè, M., Khotyaintsev, Y. V., Vaivads, A., Fuselier, S., Graham, D. B., et al. (2017). Cold ionospheric ions in the magnetic reconnection outflow region. *Journal of Geophysical Research: Space Physics*, *122*, 10,194–10,202. https://doi.org/10.1002/2017JA024287

Li, J. H., & Ma, Z. W. (2010). Nonlinear evolution of resistive tearing mode with sub-Alfvenic shear flow. *Journal of Geophysical Research*, *115*, 6–11. https://doi.org/10.1029/2010JA015315

Liang, H., Ashour-Abdalla, M., Lapenta, G., & Walker, R. J. (2016). Oxygen impacts on dipolarization fronts and reconnection rate. *Journal of Geophysical Research A: Space Physics*, *121*, 1148–1166. https://doi.org/10.1002/2015JA021747

Liang, H., Lapenta, G., Walker, R. J., Schriver, D., El-Alaoui, M., & Berchem, J. (2017). Oxygen acceleration in magnetotail reconnection. *Journal of Geophysical Research: Space Physics*, *122*, 618–639. https://doi.org/10.1002/2016JA023060

Mitchell, H. G., & Kan, J. R. (1978). Merging of magnetic fields with field-aligned plasma flow components. *Journal of Plasma Physics*, *20*(1), 31–45. https://doi.org/10.1017/S0022377800021346

Rosenbauer, H., Grünwaldt, H., Montgomery, M. D., Paschmann, G., & Sckopke, N. (1975). Heos 2 plasma observations in the distant polar magnetosphere: The plasma mantle. *Journal of Geophysical Research*, *80*(19), 2723–2737. https://doi.org/10.1029/ja080i019p02723

Roytershteyn, V., & Daughton, W. (2008). Collisionless instability of thin current sheets in the presence of sheared parallel flows. *Physics of Plasmas*, *15*(8), 082901. https://doi.org/10.1063/1.2968459

Schillings, A., Slapak, R., Nilsson, H., Yamauchi, M., Dandouras, I., & Westerberg, L.-G. (2019). Earth atmospheric loss through the plasma mantle and its dependence on solar wind parameters. *Earth Planets and Space*, *71*(1), 70. https://doi.org/10.1186/s40623-019-1048-0

Shay, M. A., Drake, J. F., Denton, R. E., & Biskamp, D. (1998). Structure of the dissipation region during collisionless magnetic reconnection. *Journal of Geophysical Research*, *103*(A5), 9165–9176. https://doi.org/10.1029/97ja03528

Shay, M. A., & Swisdak, M. (2004). Three-species collisionless reconnection: Effect of O^+ on magnetotail reconnection. *Physical Reviews and Letters*, *93*(17), 4–7. https://doi.org/10.1103/PhysRevLett.93.175001

Shuster, J. R., Chen, L. J., Hesse, M., Argall, M. R., Daughton, W., Torbert, R. B., & Bessho, N. (2015). Spatiotemporal evolution of electron characteristics in the electron diffusion region of magnetic reconnection: Implications for acceleration and heating. *Geophysical Research Letters*, *42*, 2586–2593. https://doi.org/10.1002/2015GL063601

Siscoe, G. L., Frank, L. A., Ackerson, K. L., & Paterson, W. R. (1994). Properties of the mantle-like magnetotail boundary layer: GEOTAIL data compared with a mantle model. *Geophysical Research Letters*, *21*(25), 2975–2978.

Taguchi, S., Kishida, H., Mukai, T., & Saito, Y. (2001). Low-latitude plasma mantle in the near-Earth magnetosphere: GEOTAIL observations. *Journal of Geophysical Research*, *106*(A2), 1949–1954. https://doi.org/10.1029/2000ja900100

Tenfjord, P. (2020). Replication data for interaction of cold streaming protons with the reconnection process. DataverseNO, https://doi.org/10.18710/MEYFPM

Tenfjord, P., Hesse, M., & Norgren, C. (2018). The formation of an oxygen wave by magnetic reconnection. *Journal of Geophysical Research: Space Physics*, *123*, 9370–9380. https://doi.org/10.1029/2018JA026026

Tenfjord, P., Hesse, M., Norgren, C., Spinnangr, S. F., & Kolstø, H. (2019). The impact of oxygen on the reconnection rate. *Geophysical Research Letters*, *46*, 6195–6203. https://doi.org/10.1029/2019GL082175

Toledo-Redondo, S., Dargent, J., Aunai, N., Lavraud, B., André, M., Li, W., et al. (2018). Perpendicular current reduction caused by cold ions of ionospheric origin in magnetic reconnection at the magnetopause: Particle-in-cell simulations and spacecraft observations. *Geophysical Research Letters*, *45*, 10,033–10,042. https://doi.org/10.1029/2018GL079051

Toledo-Redondo, S., Vaivads, A., André, M., & Khotyaintsev, Y. V. (2015). Modification of the Hall physics in magnetic reconnection due to cold ions at the Earth's magnetopause. *Geophysical Research Letters*, *42*, 6146–6154. https://doi.org/10.1002/2015GL065129

Wang, S., Kistler, L. M., Mouikis, C. G., & Petrinec, S. M. (2015). Dependence of the dayside magnetopause reconnection rate on local conditions. *Journal of Geophysical Research: Space Physics*, *120*, 6386–6408. https://doi.org/10.1002/2015JA021524

Wang, C. P., Lyons, L. R., & Angelopoulos, V. (2014). Properties of low-latitude mantle plasma in the Earth's magnetotail: ARTEMIS observations and global MHD predictions. *Journal of Geophysical Research: Space Physics*, *119*, 7264–7280. https://doi.org/10.1002/2014JA020060

Xu, Y., Fu, H. S., Norgren, C., Toledo-Redondo, S., Liu, C. M., & Dong, X. C. (2019). Ionospheric cold ions detected by MMS behind dipolarization fronts. *Geophysical Research Letters*, *46*, 7883–7892. https://doi.org/10.1029/2019GL083885

Zhou, M., Deng, X. H., Pang, Y., Huang, S. Y., Yuan, Z. G., Li, H. M., et al. (2012). Revealing the sub-structures of the magnetic reconnection separatrix via particle-in-cell simulation. *Physics of Plasmas*, *19*(7), 1–7. https://doi.org/10.1063/1.4739283